Method to attain substantial anchorage forces within limited embedment depths into thin fibre-reinforced concrete plates and shells

Author:

Assoc.Prof. **Niyazi Özgür Bezgin**, PhD. CE
Istanbul University - Cerrahpaşa, Avcılar Campus
Department of Civil Engineering
Istanbul, Turkiye
ozgur.bezgin@iuc.edu.tr
Corresponding author

Niyazi Özgür Bezgin

Method to attain substantial anchorage forces within limited embedment depths into thin fibre-reinforced concrete plates and shells

Contemporary fibre-reinforced concrete provides new opportunities for the design of thin concrete elements with substantial bending strength. To realise the full benefits of reduced weights owing to the reduced structural thickness, new anchorage elements must be developed that can sustain high anchorage forces within limited embedment depths in thin plates. This paper introduces a new anchorage design for concrete plates or shells that provides high tensile forces between 4 and 6 kN within a small embedment depth of 5 mm. The proposed design concept includes a two-stage anchorage mechanism that provides the required tensile strength and ductility for the anchorage. Achieving such anchorage capabilities within the limited embedment depth of thin concrete elements enables the production of lightweight concrete plates and shells.

Niyazi Özgür Bezgin

Metoda za postizanje značajnih sila sidrenja unutar ograničenih dubina ugradnje u tanke betonske ploče i ljuske ojačane vlaknima

Suvremeni beton ojačan vlaknima pruža nove mogućnosti za projektiranje tankih betonskih elemenata sa značajnom otpornošću na savijanje. Kako bi se u potpunosti ostvarile prednosti smanjenja težine zbog smanjene debljine konstrukcije, moraju se razviti novi elementi za sidrišta, koji mogu izdržati velike sile sidrenja u okvirima ograničenih dubina ugradnje u tanke ploče. Cilj ovog rada je predstaviti novi koncept sidrišta za betonske ploče ili ljuske, koji osigurava velike vlačne sile između 4 i 6 kN s malom ugradbenom dubinom od 5 mm. Predloženi projektni koncept uključuje dvostupanjski mehanizam za sidrište koji sidrištu osigurava potrebnu vlačnu čvrstoću i duktilnost. Ovakva sidra unutar ograničene dubine ugradnje tankih betonskih elemenata omogućuju proizvodnju lakih betonskih ploča i ljuski.

1. Introduction

Concrete is a versatile construction material that allows for the design of various structural shapes in response to numerous architectural needs. Contemporary concrete designs can achieve substantial levels of tensile strength by adding alkali-resistant glass, polymers, and steel fibres to the concrete mixture [1-3]. Owing to the enhanced tensile strength due to the embedded fibres in the concrete, steel reinforcement bars can be omitted, thus enabling the design of thin concrete plates and concrete shells. Concrete plates as thin as 10 mm are used to form the architectural facades of buildings [3]. These plates are designed to resist the pressures imposed by wind and the inertial forces caused by seismic events [4, 5].

Advancements in structural concrete design require a holistic view that includes the design of the structural concrete element and the support and reinforcement attachments for the designed concrete element. Improvements in concrete tensile strength through the addition of alkali-resistant glass and steel fibres eliminate the need for separate reinforcement cages to counter tensile stresses developed within certain structural concrete elements under design forces, such as the plate and shell elements of façades [6, 7]. The elimination of steel reinforcements also eliminates the need to use a concrete cover to prevent steel corrosion, thus reducing the thickness of the plate and shell and hence its structural weight [8].

The design of a structure is incomplete without considering the design of its support elements and the connection of the structure with its support elements. Ordinarily, we consider the embedment depth of the steel reinforcement within the concrete or the transfer length of the prestressing wires within the concrete, which requires a substantial mass of concrete to be embedded. However, when the available volume of a concrete structure is limited, such as in thin concrete plates and shells, and the amount of force that must be transferred is high, other methods are necessary to transfer these forces within a limited depth.

The thickness of the thin plates and shells is often increased at the anchor points to provide structural material to bond with the anchor elements. However, such methods are counterproductive for designing lightweight plates and shells, causing an increase in structural self-weight owing to the increased thickness at the support points.

This study presents the development of a new anchoring method and anchorage element for thin concrete plates and shells composed of glass-fibre-reinforced concrete. The proposed anchorage could develop substantial anchoring forces and ductility within a depth of 5 mm via shear interlocking. The anchorage design allows the manifestation of the tensile resistance of the embedded concrete element through shear interlocking with the embedded concrete. First, a presentation of the mixture design of alkali-resistant, glass-fibre-reinforced concrete material and the production of four sets of thin plates is presented. The mechanical design parameters of the concrete material are then determined through four-point bending tests carried out on these plates. Finally, the design of the anchor element, detailed results of pull-out tests

conducted on a set of anchorages embedded in concrete plates, and a discussion of these results are presented.

2. Material and method: selection of the concrete mixture and determination of its mechanical parameters

The design and testing of the proposed anchor mechanism began with the production of the design material and test samples to estimate the design parameters of the material using four-point bending tests. A series of mixture tests was performed by varying the mass proportions of fibre, sand, and cement. The proportions of fibre mass in the trials were 1 %, 2 %, and 3 % with respect to the mass per unit volume of concrete. Table 1 presents the contents and quantities of the mixture, which was prepared using a high-shear mixer. The fibres were 13-mm long and the plasticiser was a propriety-modified polycarboxylic ether (PCE) polymer-based material.

Table 1. Design concrete content for the mixture with a 3 % fibre ratio and 1:1.75 cement-to-sand ratio

Content	Quantity [kg/m³]
CEM I 52.5 R	910
Silica Sand	910
Alkali-resistant glass fibre	67
Plasticizer	9
Water	327

Following the determination of the proportions of the glass fibre-reinforced concrete mixture, the design material was used to produce three groups of 24 rectangular samples. The samples were 55-cm long and 10-cm wide and distributed in groups according to their thicknesses of 10, 20, and 30 mm. The first sample identification was the number of groups, denoted as 1, 2, and 3. Each group contained two sets of plates, denoted as 1 and 2, and each set contained four samples, denoted as A, B, C, and D. The difference between sets 1 and 2 was the difference in their production with respect to the attention paid to the fibre orientation. For the first set of samples, the concrete was randomly placed across the sample span without any additional action to achieve fibre orientation. The second set of samples was produced to achieve as much fibre alignment along the length of the plates as possible. Concrete was poured from one edge of the formwork and allowed to flow to the other. It was determined that achieving a fibre orientation perpendicular to the cross-section of the samples would generate the greatest benefit in terms of bending.

The samples were subjected to a four-point bending load test according to the specifications presented in EN 1170-5 'Precast concrete products test method for glass fibre reinforced cement-part 5: measuring bending strength - Complete bending test method'. [9]. Figure 1a shows the proposed four-point bending
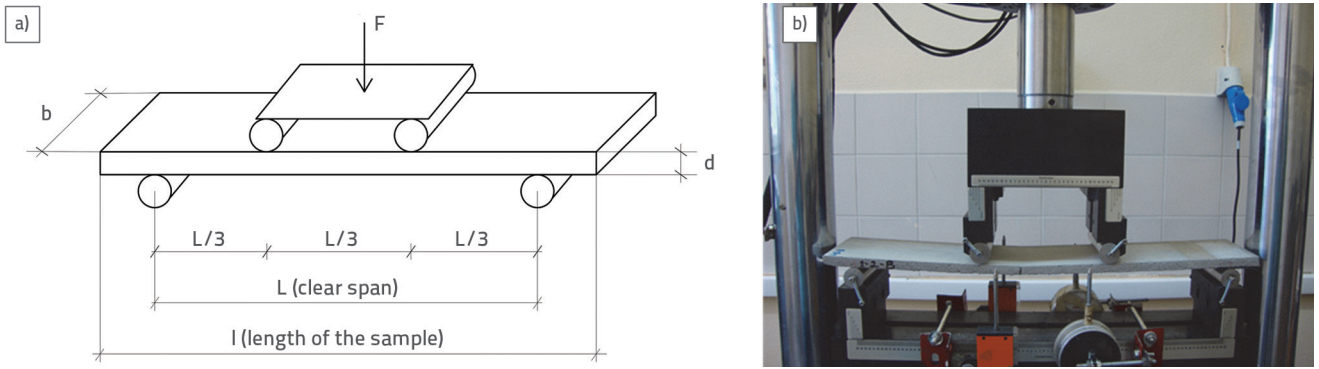
Figure 1. a) Suggested setup considering reference [9]; b) experimental setup and the four-point bending test of Sample 1-2-B

test setup, and Figure 1b shows an image of the four-point bending test for Sample 1-2-B. The width of the sample is "b" and its thickness is "d'" Sample 1-2-B is a 10 mm thick sample that was produced with care to establish the fibre orientation along the sample span. Displacement-controlled tests began with the placement of 55 cm long and 10 cm wide samples on simple supports with a clear span of 45 cm. The loading rate on the samples was 0,03 ± 0,003 mm/s, and the span was loaded at 1/3rd and 2/3rd of the span respectively. The force (F) and related deflection (Δ) data were acquired up to the limit of stress–strain proportionality (LOP) and modulus of rupture (MOR). Subsequently, the force and deflection data were used to estimate the stress values in the LOP and MOR according to Equations (1) and (2) presented in the specifications [9]. The related strains were then estimated using Equations (3) and (4) as presented in the specifications [9]. The thickness of each sample was measured at three points along its width (at the edges and centre), and the average value (d_{ave}) was used for the calculations. Equations (1) to (4) correlate the relevant stresses and strains at the elastic and ultimate limits to the section rigidity, applied force, and related deflection. The displacement-controlled bending device allowed the estimation of the cracked section rigidity through the force values measured beyond F_{LOP}.

$$\sigma_{LOP} = \frac{F_{LOP} \cdot l}{b \cdot d^2} \qquad (1)$$

$$\varepsilon_{LOP} = \frac{108}{23} \cdot \frac{\Delta_{LOP} \cdot d}{L^2} \qquad (2)$$

$$\sigma_{MOR} = \frac{F_{MOR} \cdot l}{b \cdot d^2} \qquad (3)$$

$$\varepsilon_{MOR} = \frac{108}{23} \cdot \frac{\Delta_{MOR} \cdot d}{L^2} \qquad (4)$$

Table 2 summarises the collected data and estimated stress and strain values at their respective limits.
Based on the measured forces and applied deflections, the stresses and strains were estimated and plotted, as shown in Figures 2, 3, and 4, for the three different sample thicknesses of 10, 20, and 30 mm, respectively. The bending responses to the applied deflections

were linear and elastic up to a stress limit referred to as the limit of proportionality (LOP). Following the LOP, the increase in deflections was met with a lower resistance increase rate up to a stress level (referred to as σ_2) that was measured at the intermediate level between LOP and MOR. Following this intermediate stress level, another increase in deflections resulted in even lower resistance until the highest stress level (i.e., the modulus of rupture (MOR)), at which point the samples fractured. This trilinear behaviour was observed for the three groups of samples, similar to results observed in other studies [10-14]. For each set of four samples within the group, the mean stress and respective strains were calculated, and the trilinear mean stress–strain behaviour for each set is represented in Figures 2 to 4.
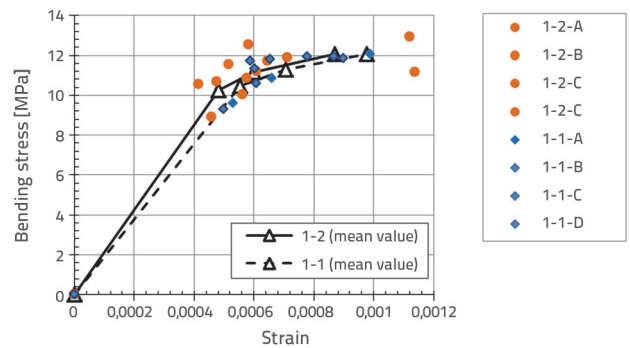

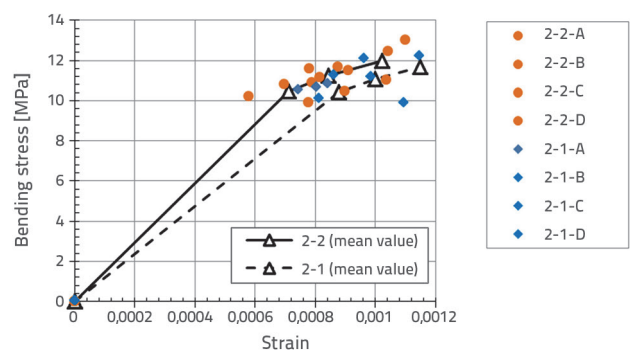Figure 2. Stress–strain curves of the two sets of 10-mm-thick samples

Figure 3. Stress–strain curves of the two sets of 20-mm-thick samples

Table 2. Summary of the test data and estimated stress and strain values

| Sample	b [mm]	d_{ave} [mm]	F_{LOP} [N]	Δ_{LOP} [mm]	F_{MOR} [N]	Δ_{MOR} [mm]	$(F_{MOR}-F_{LOP})/2$ [N]	Δ_2 [mm]	ε_{LOP}	ε_2	ε_{MOR}	σ_{LOP}	σ_2	σ_{MOR}
1-1-A	94.2	12.7	323.8	1.8	406.6	3.36	365.2	2.25	0.00053	0.00066	0.00099	9.6	10.9	12.1
1-1-B	103.1	13.3	376.6	1.62	482.3	2.82	429.4	1.97	0.0005	0.00061	0.00087	9.3	10.6	11.9
1-1-C	94.4	13	416.4	1.95	4242	2.58	420.3	2.16	0.00059	0.00065	0.00078	11.7	11.8	11.9
1-1-D	104.2	13.3	464.3	1.95	506.7	4.11	485.5	2.91	0.0006	0.0009	0.00127	11.3	11.8	12.4
1-2-A	95.8	12	329.6	1.71	360.9	231	345.2	2.18	0.00048	0.00061	0.00064	10.7	11.2	11.7
1-2-B	98.9	11.5	305.7	1.56	362	2.19	333.9	1.94	0.00042	0.00052	0.00058	10.6	11.6	12.5
1-2-C	97	12.7	308.6	1.56	386.5	3.87	347.6	1.91	0.00046	0.00056	0.00114	8.9	10	11.2
1-2-D	101.2	12.6	386.6	1.98	459.9	3.84	423.2	2.44	0.00058	0.00071	0.00112	10.9	11.9	12.9
2-1-A	99.5	22.8	1206.5	1.41	1243.1	1.59	1224.8	1.52	0.00074	0.0008	0.00084	10.5	10.7	10.8
2-1-B	99.8	22.6	1270.4	1.65	1453.9	2.43	1362.2	1.84	0.00086	0.00096	0.00127	11.3	12.1	12.9
2-1-C	96.9	22.5	1078	2.1	1182.1	2.58	1130	2.39	0.0011	0.00125	0.00135	9.9	10.4	10.8
2-1-D	101.9	22.9	1200.2	1.53	1451.9	2.16	1326.1	1.85	0.00081	0.00096	0.00115	10.1	11.2	12.2
2-2-A	93.6	21.4	1039.4	1.59	1185.2	2.1	1112.3	1.77	0.00079	0.00088	0.00104	10.9	11.7	12.4
2-2-B	104.6	21.8	1198.5	1.38	1275.7	1.8	1237.1	1.61	0.0007	0.00082	0.00091	10.8	11.2	11.5
2-2-C	94.9	22	1036.8	1.14	1322.4	2.16	1179.6	1.53	0.00058	0.00078	0.0011	10.2	11.6	13
2-2-D	103.7	21.9	1096.1	1.53	1223.8	2.04	1160	1.77	0.00078	0.0009	0.00104	9.9	10.5	11.1
3-1-A	96.9	31.3	2075.5	1.44	2075.5	1.44	2075.5	1.44	0.00105	0.00105	0.00105	9.8	9.8	9.8
3-1-B	101.3	31.5	2276	1.47	2633.1	1.86	2454.6	1.6	0.00107	0.00117	0.00136	10.2	11	11.8
3-1-C	96.6	31.5	2272.1	1.08	2453.6	1.26	2362.9	1.14	0.00079	0.00083	0.00092	10.7	11.1	11.5
3-1-D	102.6	31.8	2217.8	1.26	2217.8	1.26	2217.8	1.26	0.00093	0.00093	0.00093	9.6	9.6	9.6
3-2-A	98.6	30.9	2218.6	0.99	2505.2	1.41	2361.9	1.13	0.00071	0.00081	0.00101	10.6	11.3	11.9
3-2-B	99.2	31.4	1998.9	0.72	2386.3	1.02	2192.6	0.85	0.00052	0.00062	0.00074	9.2	10.1	11
3-2-C	100.3	30.4	2257.7	1.59	2589.1	2.1	2423.4	1.79	0.00112	0.00126	0.00148	10.9	11.8	12.6
3-2-D	96.9	31.2	2009.6	1.47	2441.9	1.83	2225.7	1.58	0.00106	0.00114	0.00132	9.6	10.6	11.6
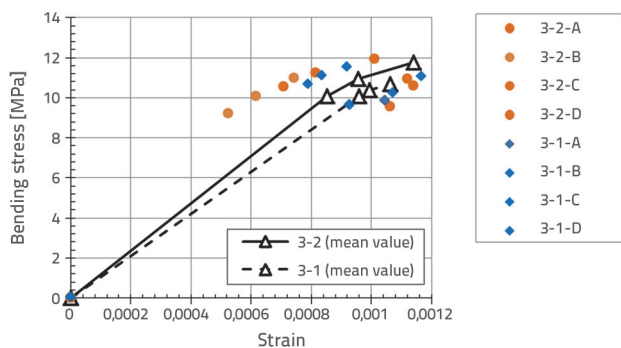
Figure 4. Stress–strain curves of the two sets of 30-mm-thick samples

Three different thicknesses representing the typical dimensions of a glass fibre-reinforced panel were used to assess the possible effects of size on the effectiveness of the fibres under bending. A comparison of Figures 2 to 4 reveals that the first set of samples with additional attention to fibre orientation showed higher stress–strain ratios in all stress–strain regions compared to samples produced without any attention to fibre orientation, which is similar to the findings of another study [15]. Figure 5 shows the variation in the average strength limits for the three distinct stress–strain regions. For each group of samples 1, 2, and 3, two different values (1 or 2) representing the two sets were presented. Each set is represented by a different colour and pattern in the figures. The effect of the fibre orientation on the stress–strain ratios beyond the limit of proportionality

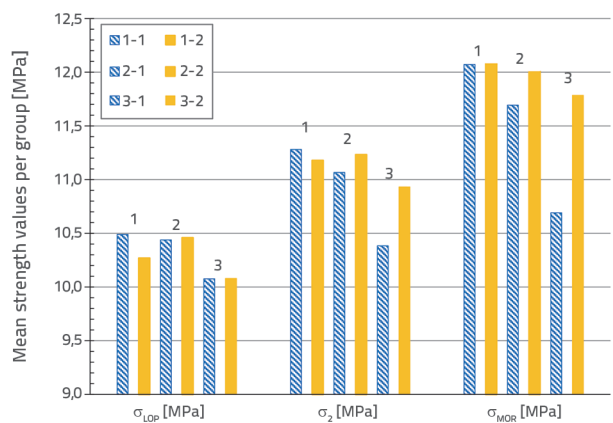is apparent in these figures for the 20 and 30 mm thick test samples.

Figure 5. Mean bending strengths at the respective limits for each group of samples

Based on the mean stress–strain plots, the stress-to-strain ratios for the respective sets were estimated. The ratio of the linear elastic stress limit to the corresponding strain is the elastic modulus of the material, which decreases with increasing strain, as shown in Figures 2 to 4. Figure 6 shows the variations in the stress–strain ratios within the respective stress–strain regions. As expected, the resistance to bending displacement decreased with increasing strain. The elastic moduli up to the LOP decreased with increasing sample thickness. The samples

reached their respective LOP values at higher strain levels as the thickness increased. For the 10 and 20 mm sample thicknesses, a fixed fibre length of 13 mm appeared to respond to the bending stresses at lower strains.
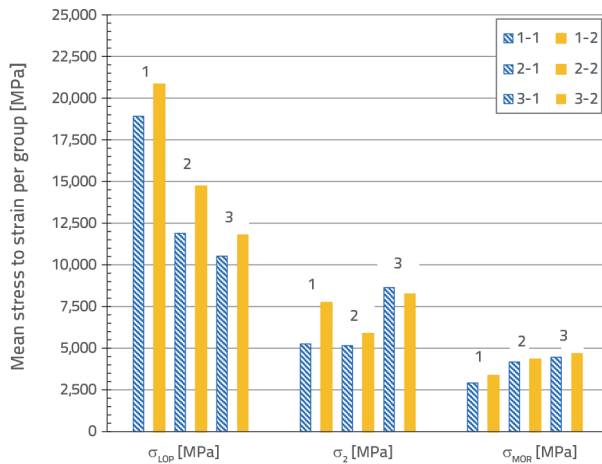

Figure 6. Estimated stress-to-strain ratios within the elastic and plastic stress–strain regions up to the respective stress limits σ_{LOP}, σ_2, and σ_{MOR}

Three compression tests carried out on standard cylinder specimens for the concrete mixtures yielded compressive strengths of 46.3, 48.1, and 45.2 MPa, respectively, with a mean value of $f_m = 46.5$ MPa and a standard deviation of SD = 1.2 MPa. The characteristic compressive strength of concrete based on 90 % confidence is $f_c = f_m - 1.28 \cdot SD = 46.5 - 1.28 \cdot 1.2 = 45$ MPa. The compression tests were conducted according to the EN 206 standard [16, 17]. The mean stress values at the limit of proportionality and at the modulus of rupture were $\sigma_{LOP} = 10.5$ MPa and $\sigma_{MOR} = 11.7$ MPa, respectively. Their standard deviations were $SD_{LOP} = 0.7$ MPa and $SD_{MOR} = 0.9$ MPa respectively.

Although concrete is mainly used for its compressive strength, its bending and direct tensile strengths are important parameters in the design of anchors in thin plates and shells [3]. However, measurement of the direct tensile strength of the concrete was not possible because a direct tensile test machine, tensile sample moulds, and sample attachments were not available during this study. Experimental investigation of the direct tensile strength is difficult, as the results can become highly dependent on the sample size and particle sizes of the components that make up the concrete mixture, as well as the loading rate [10, 12, 13]. Many researchers have investigated the relationship between the direct tensile strength and compressive strength of concrete. Based on the characteristic compressive strength $f_c = 45$ MPa, the direct tensile strength of concrete can be estimated as $f_t = 3.8$ MPa or $f_t = 4$ MPa based on CEB-FIB 91 and ACI 363R-92 standards [10]. However, these values underestimate the tensile strength of FRC because these empirical equations do not consider the effects of fibre embedment [3, 10]. Previous studies that correlated the

direct tensile strength of concrete with its bending strength determined that the direct tensile strength of fibre-reinforced concrete could be approximated as 50 % of its modulus of rupture [3, 10, 18]. The characteristic value of the modulus of rupture (f_{c-MOR}) for the design material was determined at a confidence level of 90 % as $f_{c-MOR} = \sigma_{MOR} - 1.28 \cdot SD_{MOR} = 11.7 - 1.28 \cdot 0.9 = 10.5$ MPa. Therefore, the direct tensile strength of the material used was estimated as $f_t = 0.5 \cdot 10.5$ MPa = 5.25 MPa = 5 MPa. An additional increase in the direct tensile strength is possible by using ultra-high-performance concrete that includes silica fume [19, 20]. However, the tensile strength of the material used in this study was set at the minimum value suggested for a particular fibre ratio and compressive strength of the designed concrete.

3. Design of the anchorage plate

The intended use of anchor elements is to support facade panels that are produced from thin-plate elements. The governing design force on the facade panels is the pressure caused by wind. Depending on the elevation at which the panel is installed, the architectural qualities of the parent structure, and the wind characteristics, facade panels are exposed to varying pressures that range from positive to negative values. Therefore, an ultimate design negative pressure value of 2,000 N/m^2 was specified for the anchor element as the critical design condition in this study, with a distribution of one anchor element per square meter of the façade representing an extreme case. The selected design pressure value is representative of the typical high wind pressures that can act on building façades up to 60 m in height [21]. The design mode of failure of the anchor was determined to be ductile because a brittle connection would fail instantly without warning. Therefore, the anchorage design includes features that not only provide the required strength but also the required ductility.

To this end, a wedge-shaped design was adopted for an anchor plate that was 5 mm thick, as shown in Figure 7. Initially, a square plate was designed with four internal holes and wedge-shaped perimeters (Fig. 7.a). Subsequently, a circular form was adopted because of stress concentrations at the corners of the square shape. The internal holes were used as design features for two distinct reasons. The first is to facilitate the embedding of the anchor elements in fresh concrete. The second is to provide anchorage through the direct tensile strength of the concrete through the internal wedges formed by the internal holes. The external perimeter wedges provide additional strength to the strength provided by the internal wedges. The external wedges also extended the duration of the attained tensile strength and provided ductility to the anchorage system. All these design expectations were subjected to a testing program, the details of which are presented in the next section.

Figure 8 shows the plan and cross-sectional views of the designed anchorage element. The dimensions are provided in units of millimetres. The anchor element had four internal holes with a base diameter of $D_i = 16$ mm at its bottom of the anchor element. Therefore, the area of each hole at the anchor base
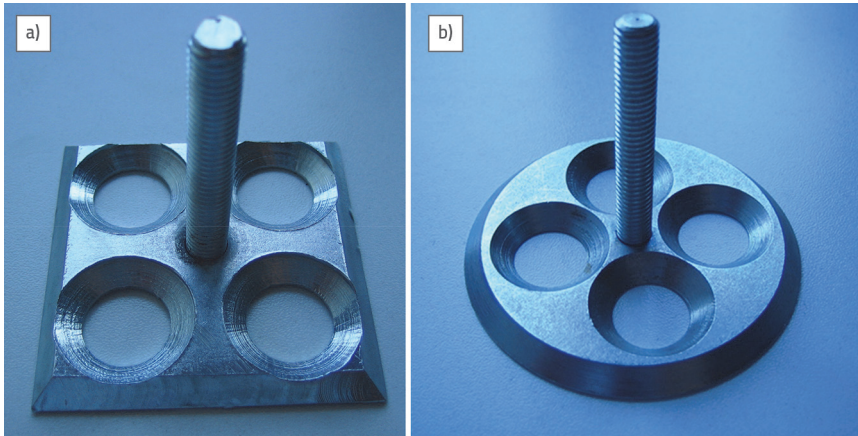
Figure 7. Prototype configuration of the anchor element: a) square formation; b) circular formation

(A_i) is therefore A_i = 200 mm². The diameter of the anchor at its base is D_b = 74 mm. Therefore, the area of the anchorage base, including the internal areas of the holes, is A_b = 4298 mm². Because there are four internal holes, the net base area of the anchorage excluding the holes is $A_n = A_b − 4A_i$ = 3498 mm². In this area, there was no bonding with concrete.

Figure 9 shows a cross-sectional elevation drawing of the anchorage, denoted as Section C Figure 8 The anchorage resistance mechanism comprises two components. The first component, denoted as R1, occurred in the internal circular holes

of the anchorage. These holes were deliberately included in the design to ensure proper anchor bonding with the concrete with minimal disruption of the concrete, and to ensure distinct internal wedge bonding that would force the concrete to crack under direct tension. The second resistance component, denoted as R2, includes the simultaneous presence of shear and tension along the inclined failure planes around the outer edges of the anchorage. R1 and R2 are not considered to occur simultaneously. The R2 activation was based on the vertical movement of the anchorage, which had to overcome R1. Therefore, R2 was considered to engage and add partially to R1, introduce ductility into the system, and improve the anchorage toughness. Hence, a perimetric anchorage is a design feature installed primarily to add ductility to the system and enhance its strength.

R1 was estimated based on the design value for the direct tensile strength (DTS$_d$) of the concrete mixture and the internal area of the hole, as shown in Equation (5).

$$R1 = DTS_d \cdot A_i = 5 \text{ MPa} \cdot 200 \text{ mm}^2 = 1000 \text{ N} \tag{5}$$

Therefore, each R1 value provided a tensile resistance of 1000 N. As the four holes were assumed to engage simultaneously, the total internal anchorage resistance was estimated using Equation (6).

$$4 \cdot R1 = 4 \cdot 1000 \text{ N} = 4000 \text{ N} \tag{6}$$

Following R1, a second estimate is made for R2. A failure plane of approximately 45° at the bottom of the anchor was assumed to surround the perimeter of the anchorage. The tests showed that the planes were inclined at approximately 30° with respect to the horizontal. The interface area along the assumed fracture perimeter is given by Equation (7).

$$A_f = \frac{\pi \cdot \left(42^2 - 37^2\right)}{cos45} = 1754 \text{ mm}^2 \tag{7}$$

Based on the direct tensile strength of the concrete and the assumed fracture area, R2 was estimated using Equation (8):

$$R2 = DTS_d \cdot A_f =$$
$$= 5 \text{ MPa} \cdot 1754 \text{ mm}^2 \tag{8}$$
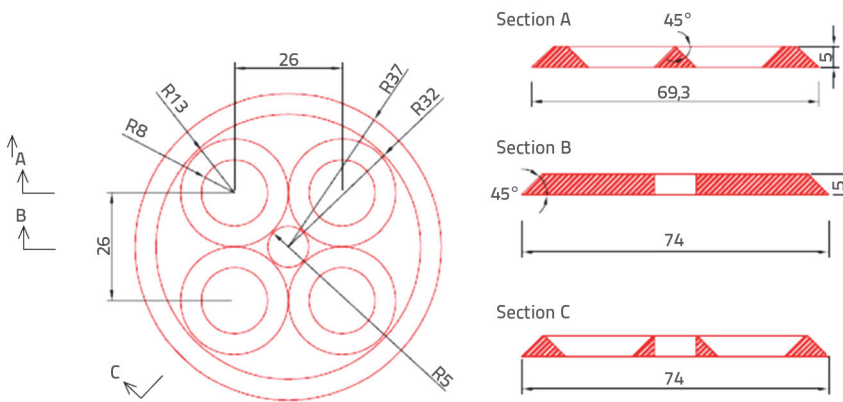$$= 8770 \text{ N}$$

Figure 8. Plan and cross-sectional views of the anchorage element with dimensions in millimetres
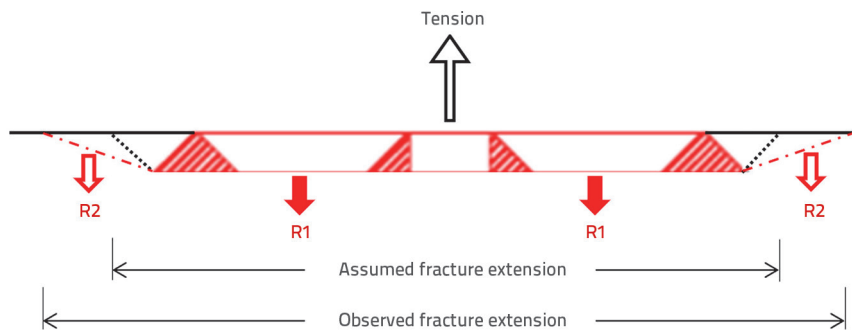

Figure 9. Schematic of the cross-section of the anchorage, highlighting the assumed and observed cones of the fractures.

However, this was the maximum possible estimate for the fractured cone, given that the full cross-section along the assumed fracture plane engaged the tension in union. This was unexpected, and the expectation was based on the presence of shear in addition to tension along the inclined fracture plane around the anchorage; failure would start gradually, engaging the interface areas consecutively rather than as a unit. Therefore, the contribution of R2 was expected to increase the ductility beyond the maximum tensile strength, which was provided by R1 and somewhat enhanced by R2. In this case, the expected capacity of the anchorages under tension was considered as a minimum $4 \cdot R1+R2 = R = 4000$ N, if any contribution from R2 was not considered. However, if part of the R2 component of the anchorage resistance can engage in addition to $4 \cdot R1$, the total anchorage pullout resistance is likely to increase beyond an estimated minimum of 4000 N. The exact behaviours of the designed anchors were observed using a series of tensile pull-out tests.

Figure 11. Embedment of square-based anchorage elements into fibre-reinforced concrete

4. Preparation and testing of the anchorage samples

Eight samples were used for the anchorage tests. Figure 10 shows the production stages of the anchorage test sample. The sample formwork was set to prepare 25-mm-thick samples followed by placing the concrete into 20 × 20 cm slots for each sample. The square sample concrete plate size was set to maintain the length-to-thickness ratio below 10 to minimise the bending effects of the plate during the tests, test the anchorages under direct tension, and maintain sufficient plate dimensions to allow physical space for the anchorage tests. An anchor element was placed on the prepared sample by gentle pressing from the top. Figure 10c shows that, as the anchorage penetrates the plate, the concrete flows out of the internal holes, easing its embedding into the concrete. The consistency of fresh concrete maintains the anchorage stability.
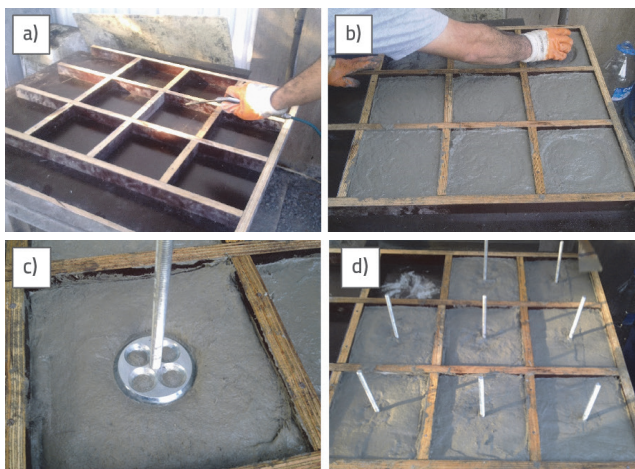

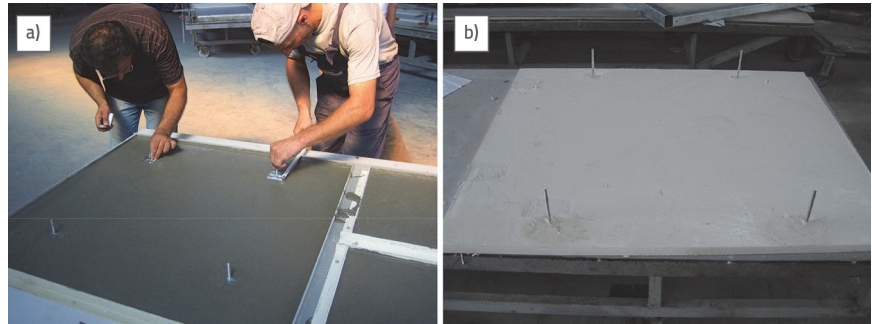Figure 10. Production stages and embedment of an anchorage test sample

The 16 mm diameters of the holes were larger than the 13 mm lengths of the fibres, preventing any adverse interference with the fibres during placement.

Figure 11 shows the production of full-scale test panels in which an anchorage is used per 0.25 m². The panel in Figure 11a was produced with ordinary CEM l, whereas the panel shown in Figure 11b was produced with white cement for the tests of the special facade support system, which is beyond the scope of this study. These figures show that the anchorage requirements of the panels were satisfied within the designed thickness of the panels without additional embedded material surrounding the anchorage points.

Figure 12 shows the setup for the displacement-controlled tensile tests. The embedded anchorage elements have a thickness of 5 mm. The anchorages were tested at a displacement rate of 1 mm/min using a load cell with a maximum capacity of 22.25 kN. Figure 13 shows a close-up view of the anchorage test showing the failed state of the anchorage.

Figure 12. Tensile testing of the embedded anchorage element

Figure 14 shows plan views of the tested samples and crack patterns. The anchors did not pull when they failed. Instead, the anchorages remained anchored within the surrounding concrete and forced the direct tensile fracture of the internal cones, followed by the circumferential volume of the concrete to rip away from the concrete plates in an approximately conical shape, as intended.
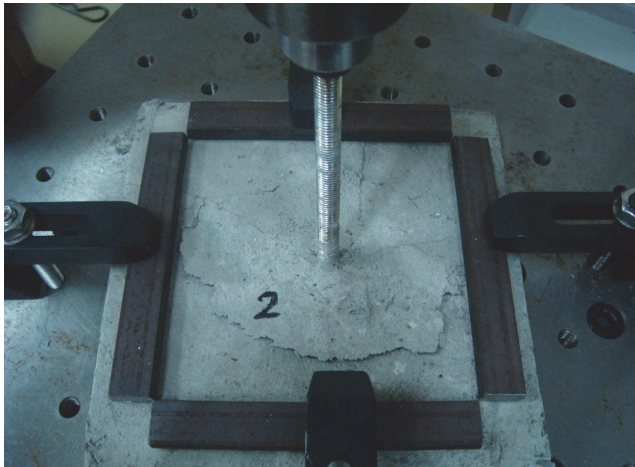
Figure 13. View of the tensile test of a specimen up to failure

tensile forces. What would normally terminate at the highest force at the respective displacement was carried out much further, albeit with a lower but persistent tensile resistance.
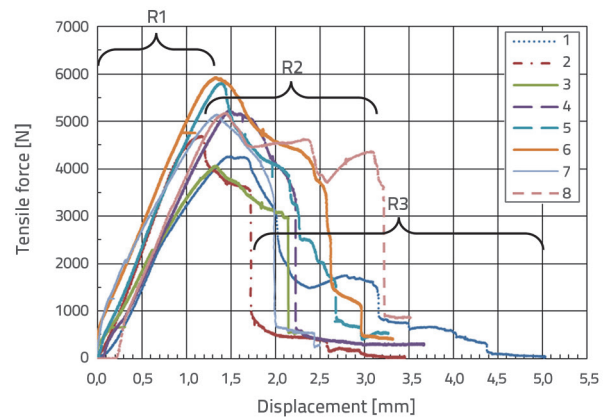

Figure 15. Force–displacement characteristics of the tested samples up to failure

Figure 15 shows the force–displacement responses of the embedded anchorages. Following an initial linear and elastic response, the anchorages exhibited expected ductility beyond the maximum forces attained until failure. The mean tensile strengths of the eight anchorages tested is F_t = 5 kN. All the anchorage forces were above the design strength of R1 = 4 kN. The additional strength beyond R1 was attributed to the variable tensile strength contributed by R2. However, the main contribution of the wedge action that developed around the anchorage perimeter was the ductility observed after anchorage displacement at the highest

For all the tested samples, three distinctively different force–displacement regions were observed. The first region, R1, exhibited a distinctively linear behaviour up to the maximum force value for all samples. The constancy of the force–displacement ratio was maintained up to the maximum force. There were slight deviations from this linearity at a 0.75 mm displacement of Samples 1 and 3. Samples 3, 5, 6, and 7 exhibited very high stiffnesses before a displacement of approximately 0.1 mm followed by a lower but linear force–displacement behaviour up to the highest tensile force. Samples 4 and 8 show a slight slip from 0.1 to 0.15 mm followed by the engagement of the linear-elastic stiffness zone after a displacement of approximately 0.3 mm. The highest tensile forces that were obtained vary between 4 and 6 kN at displacements ranging from 1.2 to 1.5 mm. Beyond these displacement limits, the second force–displacement region, R2, shows that anchorage strengths decrease by up to 40 % of their maximum values at displacements ranging from 1.7 to 2.4 mm. The abrupt termination of this second behavioural region was gradual in Samples 1 and 5, unlike the other seven samples. Only one sample, Sample 8, showed an extended second behavioural resistance up to a 3.2 mm displacement. Following the second region, the third force displacement region (R3), which starts at approximately 1.7 mm for Sample 2 and at 2 to 3.2 mm for Samples 1, 3, 4, 5, 6, 7, and 8, showed severely reduced anchor strength. However, some
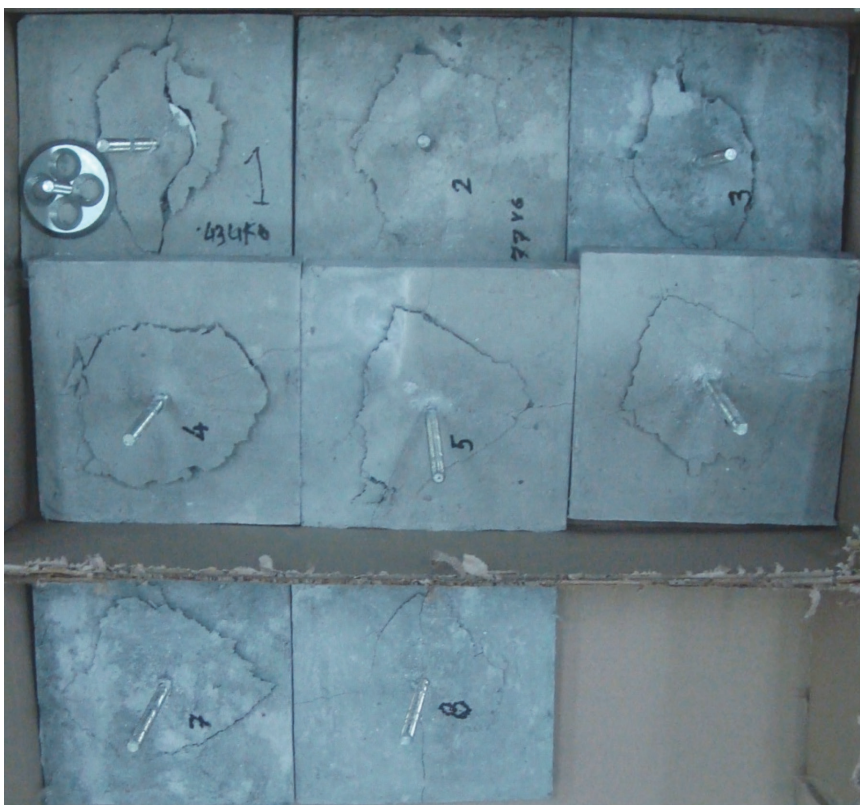

Figure 14. Plan view of the eight samples showing fracture patterns after the tensile failure tests

resistance and toughness due to fibre slippage with associated anchorage displacements was observed, extending from 3.3 to 5 mm until failure. Figure 15 shows these regions for the eight tested samples.

Figure 15 clearly show that the R1 component provided strength. This was supplemented to varying degrees by the R2 component, which was primarily responsible for the ductility observed beyond the displacement attained at the tensile strength level. Therefore, the failure of the anchors was not abrupt and occurred gradually. Figure 16 shows the maximum forces attained by the anchorages and their respective displacements. The maximum tensile pull-out force attained varies from 4060 to 5928 N. The slopes of the force-to-displacement values yielded tensile stiffness values ranged from 2911 to 4431 N/mm. The results yielded a mean tensile strength of 5 kN and mean tensile stiffness of 3.7 kN/mm. Each of the tested samples exceeded the minimum tensile strength estimate of the 4 kN design.
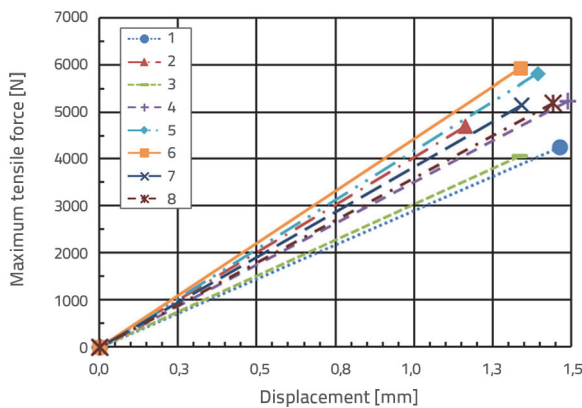

Figure 16. Linear and elastic force–displacement characteristics of the tested samples up to the highest stress limits

5. Investigation of the ductility behaviours and energy absorption capacities of the anchors

The cracked edges of the specimens exhibit circular-to-polygonal circumferential characteristics. In other words, the cracking patterns were not distinctively different from each other, indicating the homogeneity in the behaviour of the anchorages with respect to the tensile forces. Each cracked anchorage, except the first that disintegrated, was digitally photographed,

and the photographs were transferred to a computer-aided design program, where the perimeter traces were extracted, as shown in Figure 17. Table 3 lists the measured fracture areas. Figure 18 presents a bar graph of the estimated absorbed energies and fracture areas for each anchorage, and Figure 19 presents the calculated energy absorption per unit fracture area. The results for Sample 8 are highlighted for discussion in this section.
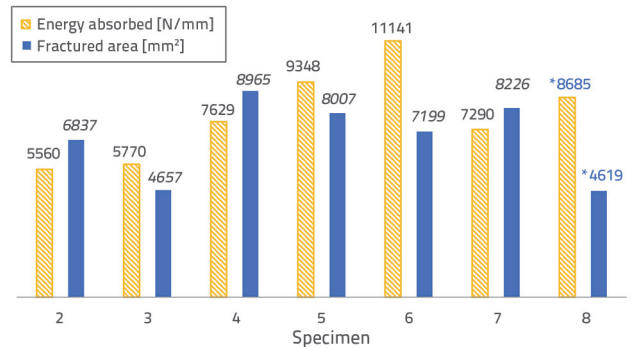

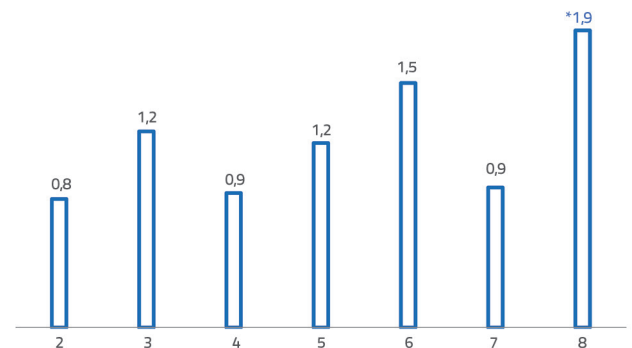Figure 18. Comparison of the energy absorbed and fractured areas for each sample

Figure 19. Energy absorbed per unit of the fracture area q (Nmm/mm²)

Samples 2, 3, 4, 5, and 7 show an average of 1 N/mm of energy absorbed per unit area. Samples 6 and 8 absorbed similar energies despite the lower fracture area of Sample 8, resulting in a higher energy absorption per unit fractured area. This is because of the peculiar force–displacement diagram of Sample 8 shown in Figure 15. The tensile resistance of Sample 8 suddenly increased at a

Figure 17. Perimeter traces of fractured anchorage for Samples 2 to 8

Table 3. Estimated interface areas of cracked anchorage concrete cone net areas

Samples	2	3	4	5	6	7	8
Areas of cracked [mm²]	6837	4657	8965	8007	7199	8226	4619

displacement value of 2.5 mm, where new fibre engagements occurred and lasted until a displacement of approximately 3 mm, after which the tensile resistance decreased significantly. This added ductility increases the energy absorption capacity. This type of tensile engagement was observed only for Sample 8. If the behaviour after a 2.5 mm displacement had not been observed and if the resistance had been terminated at a displacement value of 2.5 mm, the energy absorbed by this sample would have decreased below 8685 N/mm, and the energy absorbed per unit of fracture area would have reduced to < 1.9. Another interesting finding of the pull-out test of Sample 8 was the substantial energy absorption compared with the relatively small fracture area of

4,619 mm². In this sense, Sample 8 was very similar to Sample 3 in terms of fracture area but had almost 50 % higher energy absorption and 25 % higher tensile strength. Sample 8 is included in the above figures to highlight the behavioural characteristics of the fibre-reinforced anchorage system.

Figures 20.a to 20.d show the fractured base plates of Samples 3, 4, 5, and 8, respectively. The internal anchor points are visible, with clear internal fractured concrete diameters provided by the embedded holes. The conical extension of the fractured regions was variable, as shown in Figure 17, and it mainly contributed to the ductility of the anchorages. Unfortunately, other samples were rendered useless for photography after being mishandled when they were dropped and severely damaged during sample relocation.

Figure 21 shows close-up views of anchorage Samples 3, 4, and 8. Again, the internal wedge fractured through direct tension and the fracture around the external perimeter of the anchorages was apparent.
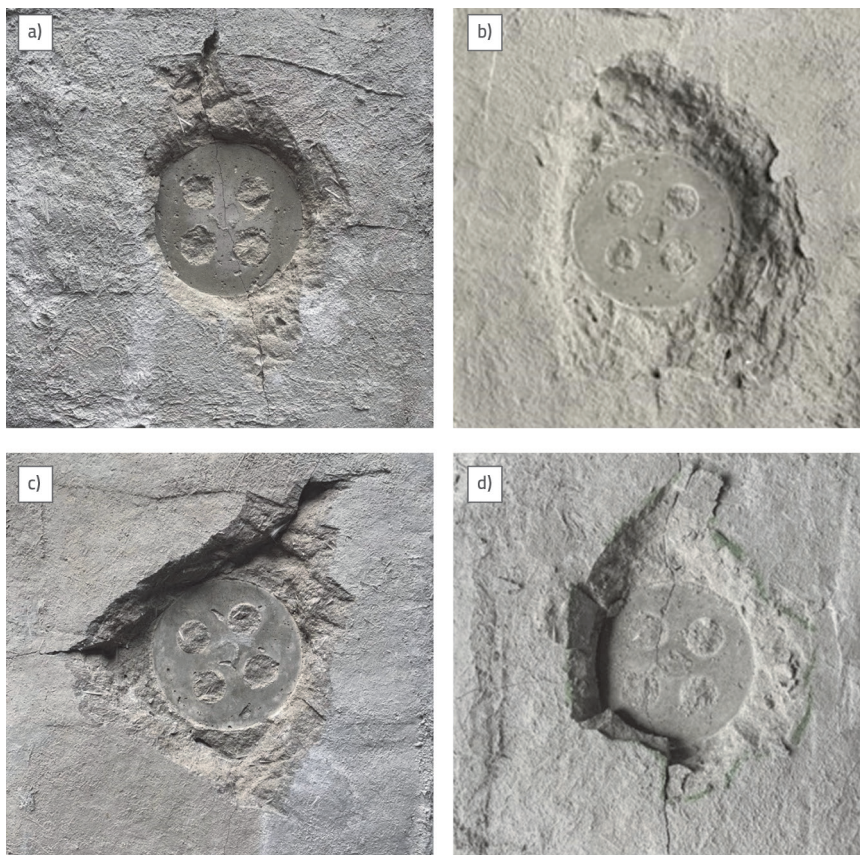

Figure 20. Crack patterns within the fractured base plates of samples: a) sample 3; b) sample 4; c) sample 5; d) sample 8
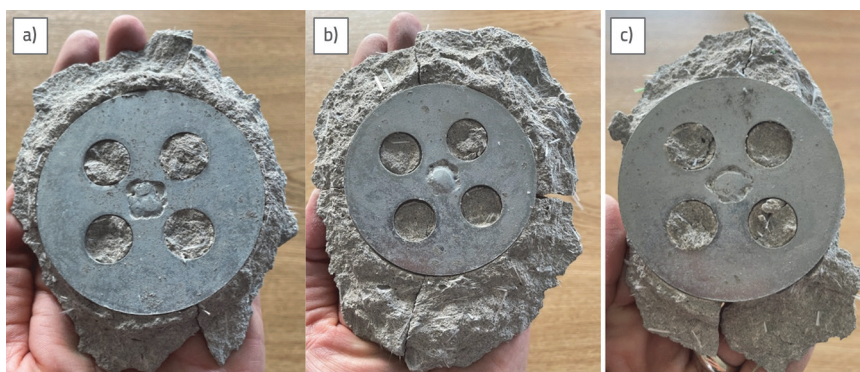

Figure 21. Close-up views of fractured anchorages in samples: a) sample 3; b) sample 4; c) sample 8

6. Conclusions

This study involved the design of an anchor element for thin fibre-reinforced concrete plates that provided strength and ductility within a limited embedment of 5 mm. The geometric values of the anchorage elements were established based on the mechanical characteristics of the embedded fibre-reinforced concrete elements. The tests verified the design principles underlying the dual-wedge design of the anchorage, which primarily provided strength through the internal wedges and ductility through the perimeter wedges. The consistency of the wedge behaviour and response under tension and the resultant tensile strength values prove valuable in providing the necessary anchoring forces for thin façade elements against negative wind pressures. The sufficiency of the limited structural thickness of the panels for anchorage embedment through the suggested anchor mechanism supports the goal of achieving a reduced panel thickness using advanced high-strength contemporary materials.

The anchorages provided a mean tensile strength of 5 kN, which is 25 % higher than the tensile strength of 4 kN. The tests indicated that the anchorage design provided substantial ductility with an energy absorption capacity with a mean value of 1 N/mm, excluding Sample 8.

Although this study provided a proof of concept and verified the hypothetical behaviour of the designed anchorage, the design tests were conducted approximately six weeks after casting the samples. The sufficiency of the designed anchorages should also be tested over time, particularly against the effects of concrete shrinkage and creep, which can cause cracks surrounding the limited embedded area of the anchorages. Possible surface cracking owing to shrinkage, creep, and temperature fluctuations can adversely affect the anchorage achieved within the suggested limited depths. If not considered, the ductility of the anchorages can decrease with time, and the anchorage strengths can be reduced. To this end, a possible second stage for future studies could include a series of tensile tests within certain long-term intervals following the production of the samples.

A second set of tests required to advance this study involves testing the anchorage systems under harmonic forces with different frequencies. Limited embedment requires an investigation of the relationship between the anchorage and embedded concrete in terms of concrete fatigue and ductility depletion. The effect of force reversals and force frequencies on the tensile force–displacement behaviour of the suggested anchorage requires a thorough investigation before the finalisation of the anchorage and any other anchorage design.

Several suggestions can be made to enhance the resilience of the anchorage against the effects of time. First, the anchorage zones of such panels should be cured and protected from the adverse effects of water seepage. Therefore, the anchorage regions should retain their water content until they are fully cured and then supplemented with liquid mineral admixtures to make them fully water- and moisture-resistant. Second, the anchor zone can be enhanced with a fibre-reinforced fabric grid close to the surface of the panels. These two simple actions can protect the anchor zone against the adverse effects of shrinkage, creep, temperature reversal, and repetitive forces.

REFERENCES

[1] Zollo, F.R.: Fibre-reinforced concrete: an overview after 30 years of development, Cement and Concrete Composites, 19 (1997) 2, pp. 107-122.

[3] Zhao, C., Zhu, Z., Guo, Q., Zhan, Y., Zhao, R.: Research on fiber reinforced concrete and its performance prediction method and mix design method, Construction and Building Materials, 365 (2023).

[4] Practical Design Guide for Glass Fibre Reinforced Concrete (GRC) Using Limit State Theory. The International Glassfibre Reinforced Concrete Association (GRCA), 2018.

[5] Stathopoulos, T., Zhu, X.: Wind pressures on building with appurtenances, Journal of Wind Engineering and Industrial Aerodynamics, 31 (1988) 2-3, pp. 265-281.

[6] Grosso, M.: Wind pressure distribution around buildings: a parametrical model., Energy and Buildings, 18 (1992) 2, pp. 101-131.

[7] Tóth, M., Bokor, B., Sharma, A.: Anchorage in steel fiber reinforced concrete – concept, experimental evidence and design recommendations for concrete cone and concrete edge breakout failure modes, Engineering Structures, 181 (2019), pp. 60-75.

[8] Anil, Ö., Belgin, Ç.M.: Anchorages Effects on CFRP-to-concrete Bond Strength, Journal of Reinforced Plastics and Composites, 29 (2010) 2-3, pp. 539-557.

[9] Shin, H., Kim, K., Oh, T., Yoo, D.: Effects of fiber type and specimen thickness on flexural behavior of ultra-high-performance fiber-reinforced concrete subjected to uniaxial and biaxial stresses, Case Studies in Construction Materials, 15 (2021).

[10] EN 1170-5 Precast concrete products-test method for glass fibre reinforced cement-part 5: measuring bending strength, Complete bending test, method, 24.03.1999.

[11] Le, A.T., Hoang, A.L.: Comparisons of flexural, split tensile, double punch, and direct tension tests on high-performance concrete reinforced with different fiber types, Case Studies in Construction Materials, 19 (2023).

[12] Gao, D., Lv, M., Wei, D., Pang, Y., Tang, J.: Trilinear tensile stress–strain constitutive model for high ductility cementitious composite with totally recycle fine aggregate, Construction and Building Materials, 319 (2022).

[13] Zheng, D., Wu, R., Sufian, M., Kahla, N.B., Atig, M., Deifalla, A.F., Accouche, O., Azab, M.: Flexural Strength Prediction of Steel Fiber-Reinforced Concrete Using Artificial Intelligence, Materials, 15 (2022) 5194.

[14] Hu, H., Wang, Z., Figueiredo, F.P., Papastergiou, P., Guadagnini, M., Pilakoutas, K.: Postcracking tensile behavior of blended steel fiber-reinforced concrete, Structural Concrete, 20 (2019) 2, pp. 707-719.

[15] Pekgokgoz, R.K., Avcil, F.: Effect of steel fibres on reinforced concrete beam-column joints under reversed cyclic loading, GRAĐEVINAR, 73 (2021) 12, pp. 1185-1194, https://doi.org/10.14256/JCE.3092.2020

[16] Zerbino, R., Tobes, J.M., Bossio, M.E., Giaccio, G.: On the orientation of fibers in structural members fabricated with self-compacting fiber-reinforced concrete. Cement and Concrete Composites, 34 (2012) 2, pp. 191-200.

[17] EN 206: Concrete – Specification, performance, production and conformity, 2013.

[18] EN 206 Conformity testing for concrete strength in compression, Procedia Engineering, 171 (2017), pp. 227-237.

[19] Oettel, V., Schulz, M., Haist, M.: Empirical approach for the residual flexural tensile strength of steel fiber-reinforced concrete based on notched three-point bending tests, Structural Concrete, 23 (202), pp. 993–1004.

[20] Natarajan, S., Murugesan, A., Dhanapal, J., Narayanan, A.: Glass fiber reinforced ultra-high strength concrete with silica fume, GRAĐEVINAR, 74 (2022) 10, pp. 849-856, https://doi.org/10.14256/JCE.3431.2021

[21] Choi, D., Hong, K., Ochirbud, M. et al.: Mechanical Properties of Ultra-High Performance Concrete (UHPC) and Ultra-High Performance Fiber-Reinforced Concrete (UHPFRC) with Recycled Sand. International Journal of Concrete Structures and Materials, 17 (2023) 67.

[22] Istanbul Metropolitan Municipality, Istanbul High Rise Buildings Wind Load Specification, Kandilli Observatory and Seismic Research Institute, Boğaziçi University, August 2009.